Journal of Alloys and Compounds 509 (2011) 3457–3467

Contents lists available at ScienceDirect

Journal of Alloys and Compounds

journal homepage: www.elsevier.com/locate/jallcom

Synthesis and on-line ultrasonic characterisation of bulk and nanocrystalline $La_{0.68}Sr_{0.32}MnO_3$ perovskite manganite

K. Sakthipandi[a], V. Rajendran[a,*], T. Jayakumar[b], Baldev Raj[b], P. Kulandivelu[c]

[a] Centre for Nano Science and Technology, K S Rangasamy College of Technology, Tiruchengode 637215, Tamil Nadu, India
[b] Indira Gandhi Centre for Atomic Research, Kalpakkam 603102, Tamil Nadu, India
[c] Department of Mechanical Engineering, K S Rangasamy College of Technology, Tiruchengode 637215, Tamil Nadu, India

ARTICLE INFO

Article history:
Received 29 August 2010
Received in revised form
17 December 2010
Accepted 17 December 2010
Available online 28 December 2010

Keywords:
Ultrasonic velocities
Attenuations
Perovskite
Structural transition
Curie temperature

ABSTRACT

$La_{0.68}Sr_{0.32}MnO_3$ perovskite manganite samples were prepared using sonochemical reactor and solid state reaction technique. The ultrasonic velocity, attenuation and elastic moduli of samples were measured using ultrasonic through transmission method, at a fundamental frequency of 5 MHz over a wide range of temperatures. The temperature dependence of the ultrasonic parameters shows an interesting anomaly in all the compositions. The observed dramatic softening and hardening in sound velocities or attenuation is related to phase transitions. The linear magnetostriction effect is more dominant in the perovskite than volume magnetostriction effect which is evident from the observed anomalous in both longitudinal and shear velocities and attenuation. Further, a decrease in grain size in the sintered sample leads to a shift in the ferromagnetic transition temperature (T_C) from 375 to 370 K.

1. Introduction

Over the past few years, perovskite manganites $R_{1-x}A_xMnO_3$ (where R trivalent rare earth elements and A divalent alkaline earth ions) were attracted for potential applications like solid oxide fuel cells, magnetic sensors/reading heads and frequency switching devices due to their unique physico-chemical [1–3], and giant magneto resistance (GMR) properties [4–8]. In perovskite magnetic materials, particularly $La_{0.68}Sr_{0.32}MnO_3$ (LSMO) perovskite, the existence of highest value of Curie temperature (T_C) and very low carrier density with a high spin polarisation of charge carriers make them very promising candidate for room temperature applications. Thus, it is interesting to explore the influence of particle size on the exotic properties of perovskite magnetic materials. The enhancement in the optical, resistivity, thermal and magnetic properties of materials by reduction in particle sizes is well proven in nanostructured materials. The nanostructured materials are used to widen the opportunities to improve the catalytic activity in solid fuel cells [9].

A variety of methods are available such as co-precipitation [8,10], sol–gel [11], hydrothermal [12], ball mill [13], spray pyrolysis [14], pulse laser deposition [15], molecular beam epitaxy [16], magnetron sputtering [17], metal–organic decomposition [18], electrochemical deposition [19] and aerosol pyrolysis [20] to prepare the nanosized LSMO perovskite materials. The sonochemical method is one of the simple techniques which are successfully employed to prepare highly pure and homogeneous nanostructured powders [19]. Some of the drawbacks of possible inhomogeneities in the co-precipitation method are overcome in sonochemical method. This is achieved by forming the homogenous colloidal suspension in liquid phase of perovskite manganites [19].

In LSMO perovskite materials, the co-existence of Mn in both Mn^{3+} and Mn^{4+} states facilitates to maintain the charge neutrality. In Mn^{3+}, the electrons are disturbed in lower triplet t_{2g} states and one electron in the existing three d-electrons is disturbed in lower t_{2g} states, leaving the e_g state vacant [21]. The transitions between the above levels are responsible for ferromagnetic (FM) to paramagnetic (PM) and metal insulator (MI) transitions [21]. Attempts have been made to study the colossal magneto resistance (CMR), charge ordering (CO), metal–insulator (MI) transition, antiferromagnetic (AFM) to ferromagnetic (FM) phase transition, lattice dynamics, structural changes, electrical properties, magnetic properties, transport properties, etc., in LSMO perovskite through different measurement techniques like electrical resistivity, magnetoresistance, magnetisation, specific heat and ultrasonic studies [21,22]. Even though different techniques are available, on-line ultrasonic studies is a unique and impor-

---

* Corresponding author. Tel.: +91 4288 274741–4/880; fax: +91 4288 274870/860.
E-mail address: veerajendran@gmail.com (V. Rajendran).

0925-8388/$ – see front matter © 2010 Elsevier B.V. All rights reserved.
doi:10.1016/j.jallcom.2010.12.148

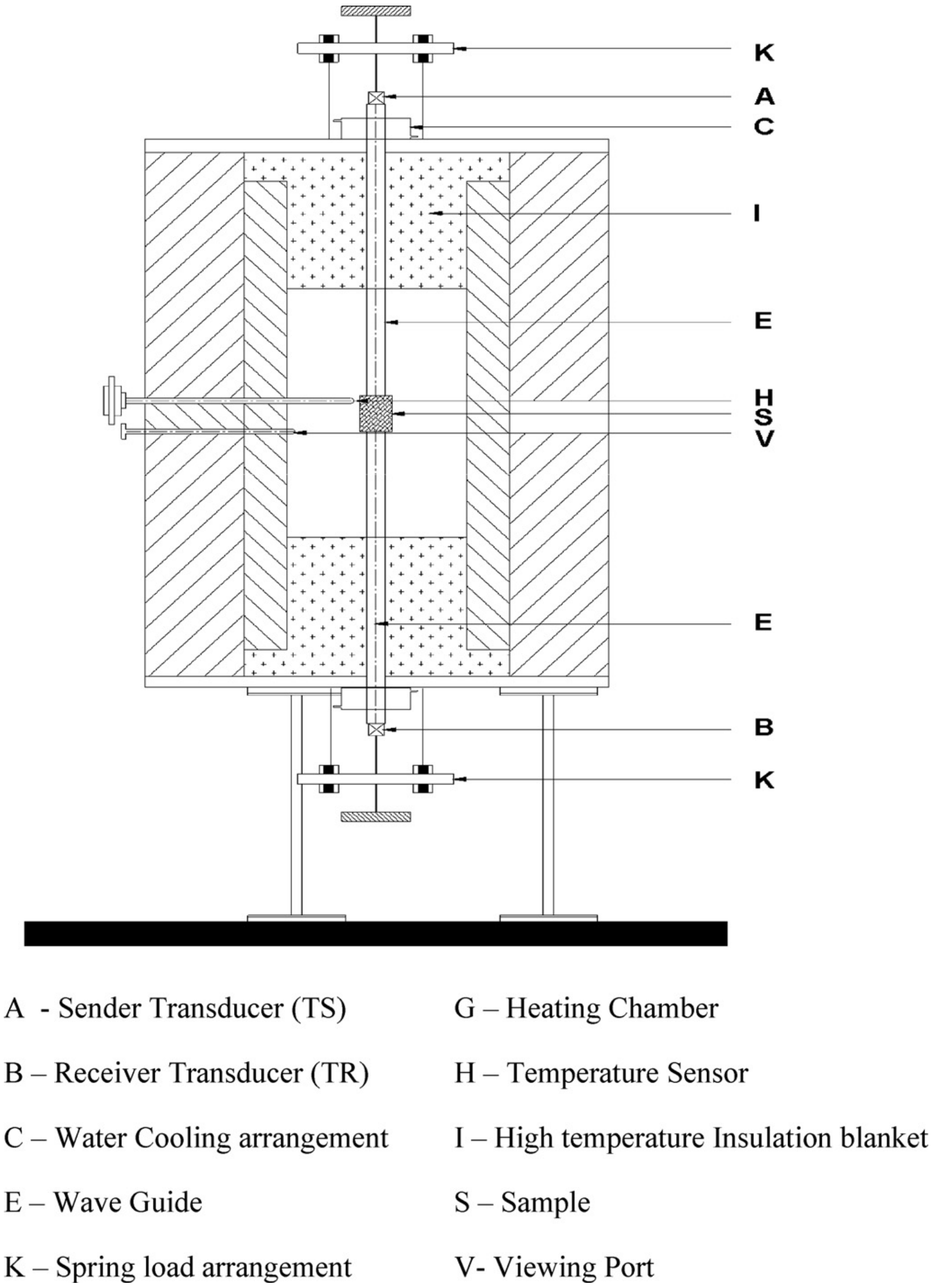

Fig. 1. Cross-sectional view of high temperature experimental set-up employing through transmission technique and mechanical arrangement of the specimen, waveguide and transducer.

tant tool used to explore the structural and phase transitions in perovskite magnetite materials. This is possibly due to the interactions of ultrasonic waves with the macroscopic, microscopic and submicroscopic particles [22–24] in the perovskite materials.

The interactions between the conduction electrons through phonons are studied employing the relative change in sound velocity as a function of temperature in $La_{0.5}Sr_{0.5}MnO_3$ [25]. The on-line ultrasonic velocity, attenuation and the derived acoustical parameters are widely used to explore phase transitions like Neel temperature (T_N), Curie temperature (T_C), charge ordering temperature (T_{CO}), etc., in the temperature region between 77 and 270 K in perovskite magnetic materials [26], $Nd_{1-x}Sr_xMnO_3$ ($x = 0.31$, 0.35, 0.37, 0.39 and 0.41) [27], $La_{1-x}Ca_xMnO_3$ ($x = 0.19$ and 0.82) [28] and $La_{0.67}Ca_{0.33-x}Sr_xMnO_3$ ($x = 0$, 0.09, 0.13, 0.33) [29]. These studies revealed that on-line ultrasonic characterisation is a versatile tool used to explore the phase and structural transitions in solid materials particularly perovskite maganities [30].

Therefore, in the present investigation, an attempt has been made to prepare bulk and nanocrystalline $La_{0.68}Sr_{0.32}MnO_3$ perovskite magnetic materials employing the sonochemical reactor and to study the structural and phase transitions employing on-line ultrasonic velocities, attenuation, and its derived elastic moduli. In addition, the observed results are compared with the bulk LSMO perovskite materials in terms of the change in the magnitudes of various physico-chemical properties.

2. Experimental procedure

2.1. Sample preparation – bulk material

The bulk sample of $La_{0.68}Sr_{0.32}MnO_3$ perovskite was prepared by a solid state reaction method. The required stoichiometric amount of high pure grade lanthanum nitrate (99.999%, Sigma–Aldrich), manganese carbonate (99.9%, Sigma–Aldrich) and strontium nitrate (99.0%, Himedia GR) powders were weighed using a digital balance and then mixed in an agate mortar. The mixed powder was ground to obtain fine powders. The ground mixture was calcinated at 600 °C in air for 2 h and then further ground to obtain a homogenous mixture. The mixture was again calcinated at 600 °C in air for 2 h. The calcinated powder was pressed into a pellet with a diameter of 13 mm and thickness of 1.3 mm using stainless steel dye. The obtained pellet was sintered at 1000 °C for 12 h in atmospheric air. The sintered pellet (hereafter known as bulk sample) was used for on-line high temperature ultrasonic velocities and attenuation measurements.

2.2. Sample preparation – nanophase material

High pure chemicals namely lanthanum nitrate (99.999%, Sigma–Aldrich), manganese carbonate (99.9%, Sigma–Aldrich) and strontium nitrate (99.0%, Himedia GR) were used as a precursor for the preparation of $La_{0.68}Sr_{0.32}MnO_3$ perovskites. The solution of lanthanum nitrate, manganese carbonate and strontium nitrate were mixed together at the required proportions to get $La_{1-x}Sr_xMnO_3$ perovskite. Initially, manganese carbonate was sonicated in dilute nitric acid for 20 min to convert the insoluble carbonate into soluble nitrate. A high intense sonication was carried out with high intensity titanium horn operated at a frequency of 20 kHz (Sonics, USA). Lanthanum nitrate and manganese nitrate salt solutions were added to the manganese solution during the sonication process. After the reaction, the pH vale of the solution was adjusted to ∼7. The temperature of the sonication was kept constant at 80 °C. After the sonication, the solution was allowed to dry in a hot air oven at a constant temperature of 120 °C for 24 h. The black residue formed was collected and then calcinated in air at 600 °C for 2 h. The calcinated powder (hereafter known as as-prepared sample) was pressed into a pellet with a diameter of 13 mm and thickness of 1.3 mm using stainless steel dye. The obtained pellet was sintered at 1000 °C for 12 h in atmospheric air. The sintered pellet (hereafter known as sintered sample) was used for on-line high temperature ultrasonic velocities and attenuation measurements.

2.3. Design and fabrication of high temperature experimental set-up

The cross-sectional view of the high temperature experimental set-up used for on-line ultrasonic velocity and attenuation measurements employing through transmission technique is shown in Fig. 1. This indigenous experimental set-up is the third version of the design overcoming various drawbacks of the previous two versions [31,32]. The diameter of the recrystallised rod was reduced to 15 mm from 25 mm which in turn reduces the volume of the furnace. Hence, it prevents the dissipation of heat to surroundings and in turn, requires less time to raise the temperature of the sample. Further, a reduction in waveguide diameter (15 mm) helps to reduce the loss of ultrasonic energy and hence, the shear wave is propagated through the waveguides easily up to 1200 K. In order to avoid the sidewall reflections of the ultrasonic waves, a notch with 7 cm depth and 5 cm width was made at the one end of the waveguide which is in contact with the sample. A sample viewing port was included in the furnace to view the sample during the on-line high temperature measurements. The necessary radiation shielding was provided to arrest even small amount of radiation reaching the transducers on both ends.

The designed furnace was vertical split type with outer shell made out of stainless steel insulated with Kanthal fibrothal backup ceramic fiber blankets to eliminate the thermal losses. The main chamber of the furnace was heated by a superior grade Kanthal super grade element (Grade F3 with Kanthal A1 embedded elements) capable of handling operating temperature up to 1400 K on a continuous basis. The power to the heating element was fed through a thyristor power control device employing a programmable temperature controller (2604, Eurotherm, USA). A temperature sensor (Duplex, K-type) which was kept very close to the sample was used to monitor the temperature of the sample. Recrystallised alumina rod (AD 998 grade, Coors tek, USA) with mirror finished ends was used as a waveguide, which has less temperature gradient and negligible scattering effects for ultrasonic waves. The water cooling arrangements employed at outer ends of the waveguides, shown in Fig. 1, guard the transducers from thermal radiations at high temperature. The furnace has the facilities for holding ultrasonic transducers at both ends of the waveguides. An adjustable spring loading arrangement is used for applying uniform pressure at the top surface of the transducers (Fig. 1).

The transducers are mounted on the probe holder and then, the parallelism is achieved. The probe holder can be moved up or down by adjusting the screw arrangements. This helps to bring the transducers, waveguides and sample all in a line and also provides a good contact and uniform pressure between different media such as waveguides, sample and transducers.

Fig. 2. Experimental arrangement for on-line ultrasonic velocities and attenuation measurements over a wide range of temperatures.

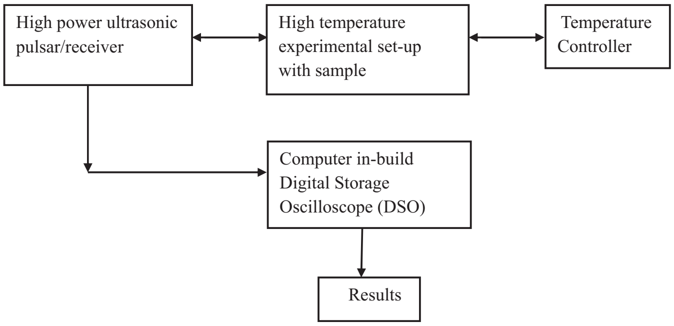

Fig. 3. Block diagram of the experimental set-up used for ultrasonic velocities and attenuation measurements.

2.4. Instrumentation

A high power ultrasonic Pulser Receiver (5900 PR, Olympus NDT, USA) and a digital storage oscilloscope (DSO) (Wave Runner 104 MXi, 1 GHz, Lecroy, USA) were employed for recording ultrasonic (rf) signals. The transducer operating at 5 MHz was used for the generation and reception of ultrasonic waves (both longitudinal and shear waves). The block diagram and the photograph of the experimental set-up used for ultrasonic measurements are shown in Figs. 2 and 3, respectively. The transducers were connected to the ultrasonic pulser receiver. In the present experimental set-up, one can obtain the required temperature either by dynamic mode or static mode of operation depending on the requirements, employing Eurotherm temperature controller. The accuracy of the temperature in the sample region is ±1 K. One can measure on-line ultrasonic velocities and attenuation from the room temperature to 1200 K at the required rate of heating.

2.5. Ultrasonic velocity and attenuation measurements

In order to provide proper impedance matching and a good contact between the sample, waveguides and transducers for the propagation of ultrasonic waves into the sample, the opposite surfaces of both the sample and the waveguides were highly polished. Through transmission technique was employed for the ultrasonic velocities and attenuation measurements. In the absence of the sample, ultrasonic waves transmitted by the sending transducer (T_S) travel along the waveguides and the waves were received by the receiving transducer (T_R), as shown in Fig. 4(a), even though some of them get reflected back to sending transducer. Thus, the transit time (t_1) through the wave guides was determined. Then, the sample is introduced between the two waveguides without disturbing the buffer rods and transducers (Fig. 4(b)). The transducer is coupled to the sample using a suitable couplant in order to get a steady back wall echo train which provides good impedance matching between the transducer, the sample and the waveguide. The transmitted pulses get shifted by a small distance. During the above process, some of the waves get reflected back into the first buffer rod and a part was transmitted into the sample. Further, reflection takes place at this stage and additional attenuation of the signal that is transmitted into the second waveguide takes place. The ultrasonic waves transmitted into the second waveguide were received by the transducer (T_R) and the corresponding transit time (t_2) was determined. The difference between the transit times t_1 and t_2 gives the transit time $\Delta t = (t_2 - t_1)$ for the ultrasonic waves in

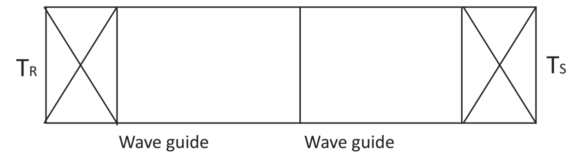

(a) Without sample

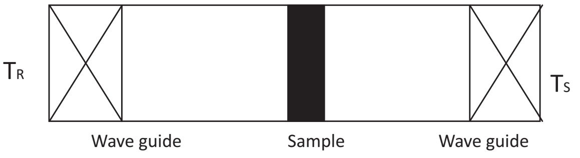

(b) With sample

Fig. 4. Through transmission technique – ultrasonic velocity and attenuation measurements.

the sample [31–33]. By the relative measurements, scattering was not considered as a major factor.

The ultrasonic velocity was measured using the following relation:

$$U = \frac{d}{\Delta t} \tag{1}$$

Knowing the sample thickness (d) in micron resolution and transit time (Δt) in nanosecond resolution, the overall accuracy obtained in the measurement of velocity is ±5 m s^{-1}. The attenuation of the ultrasonic waves in the sample was measured using the relation [31–33]:

$$\alpha(f) = \frac{1}{d}\left(\ln T + \ln\left(\frac{A_w(f)}{A_s(f)}\right)\right) \tag{2}$$

where $A_w(f)$ refers to the amplitude of the received signal with the waveguides only and $A_s(f)$ refers to the amplitude of the received signal when the sample was inserted between the wave guides. In the present study, the first and second back wall echoes were used.

$$T = \frac{4Z_wZ_s}{(Z_w + Z_s)^2} \tag{3}$$

where T is the transmission coefficient at the sample and waveguide interface, Z_w and Z_s are the acoustic impedance of the waveguide and the sample, respectively. The percentage error in the attenuation measurement is ±2%. The couplant correction for velocity and attenuation was carried out by the standard procedure [34].

2.6. Density measurements

The following relation based on the Archimedes principle was employed to measure the density of bulk and sintered sample using CCl_4 as a buoyant [31,32]

$$\rho = \frac{W_a}{W_a - W_b} x\rho_b \tag{4}$$

where W_a is the sample weight in air, W_b the sample weight in buoyant and ρ_b the density of the buoyant. A digital balance (Sartorius, Germany) was employed to measure the weight of the sample. The accuracy in the measurement of weight is ±0.1 mg. Therefore, the percentage error in the measurement of density is ±0.05.

2.7. X-ray diffraction analysis

The crystal structures of the as-prepared and sintered perovskite samples were examined by recording the X-ray diffraction (XRD) patterns using the powder X-ray diffractometer (XRD) (X' Pert Pro, Analytical, Netherlands). The XRD patterns were obtained using Cu Kα as a radiation source by applying voltage and current ratings of 40 kV and 30 mA, respectively, in the scan range of 10–80° with an increment of 0.05°.

2.8. Fourier transformation infra red spectroscopy analysis

Fourier transformation infra red (FTIR) absorption spectra of the as-prepared perovskite were recorded at the room temperature from 4000 to 400 cm^{-1} using an FTIR spectrometer (Spectrum 100, PerkinElmer, USA). The sample and high spectrum grade KBr were mixed with 1:100 weight ratios in an agate mortar and then, pressed into a pellet of 13 mm diameter and 0.5 mm thickness. FTIR studies were made in the as-prepared LSMO samples.

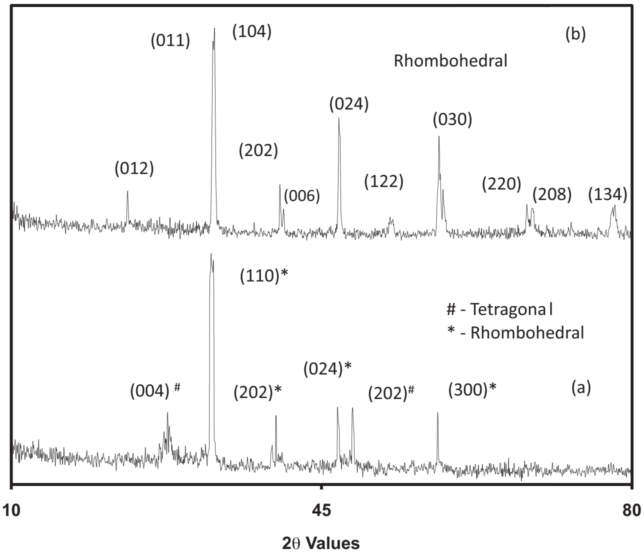

Fig. 5. XRD pattern of (a) as-prepared and (b) sintered LSMO perovskite maganities.

2.9. Microscopic studies

The scanning electron microscope (SEM) coupled with the energy-dispersive analysis X-rays (EDAX) (JEOL, JSM 5300) was used to obtain surface image of the as-prepared and sintered samples to explore morphology, microstructure and composition of perovskites samples. Similarly, transmission electron microscope (TEM, Philips, CM 200, USA) was used to obtain the substructural information and particle size of the as-prepared and sintered perovskite samples.

2.10. BET surface area analysis

The surface area measurements of the as-prepared and sintered perovskite samples were made by BET surface area analyser (Quantachrome, Autosorb-1b, USA) using nitrogen adsorption–desorption method at liquid nitrogen gas. Before starting the analysis, the sample was degassed at 463 K for 3 h to remove the physically absorbed gas molecules and moisture. The specific surface area of the prepared and sintered samples of the perovskites was measured through BET studies.

2.11. Elastic moduli

Elastic moduli of the bulk and sintered samples were obtained from the measured ultrasonic velocities (U_L and U_S) and density (ρ), employing the following relations [31,32]:

$$\text{Longitudinal modulus}: \quad L = U_L^2\rho \tag{5}$$

$$\text{Shear modulus}: \quad G = U_S^2\rho \tag{6}$$

$$\text{Bulk modulus}: \quad K = L - \left(\frac{4}{3}\right)G \tag{7}$$

$$\text{Young's modulus}: \quad E = (1+\sigma)2G \tag{8}$$

$$\text{Poisson's ratio}: \quad \sigma = \frac{L-2G}{2(L-G)} \tag{9}$$

3. Results and discussion

The recorded XRD patterns of as-prepared and sintered samples are shown in Fig. 5. It is inferred that the observed XRD patterns of the as-prepared sample reveals a crystalline nature as reported elsewhere [8,19]. Further, XRD peaks reveal the existence of mixed crystalline nature namely rhombohedral and tetragonal crystalline phases in the as-prepared sample. The peaks observed at 27.616° and 48.365° correspond to tetragonal phase and other peaks correspond to rhombohedral phase (JCPDS file nos.: 89-4461 and 51-0118). On the other hand, rhombohedral phase with the

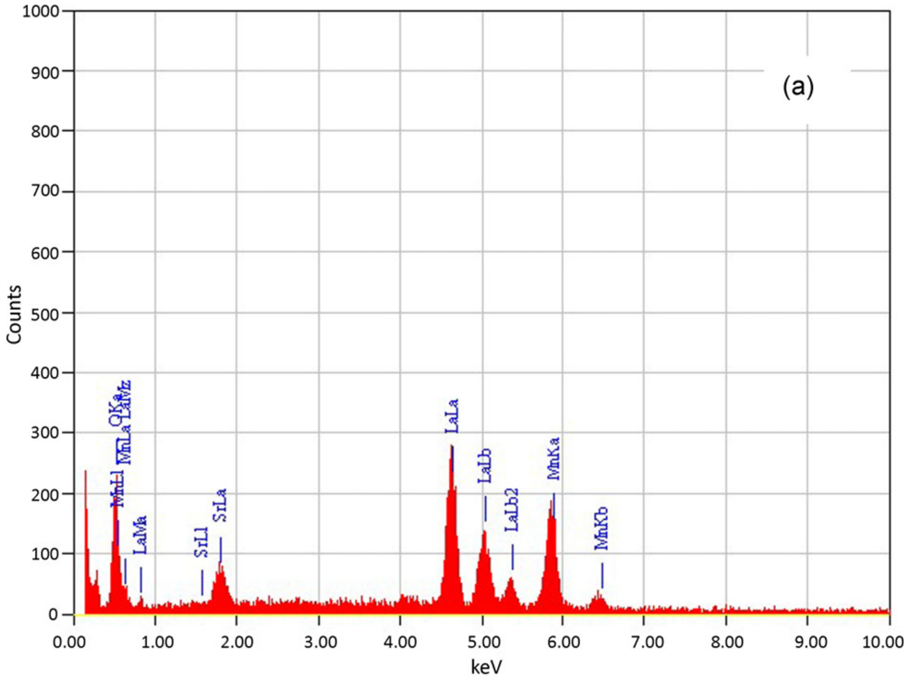

(a) As-prepared

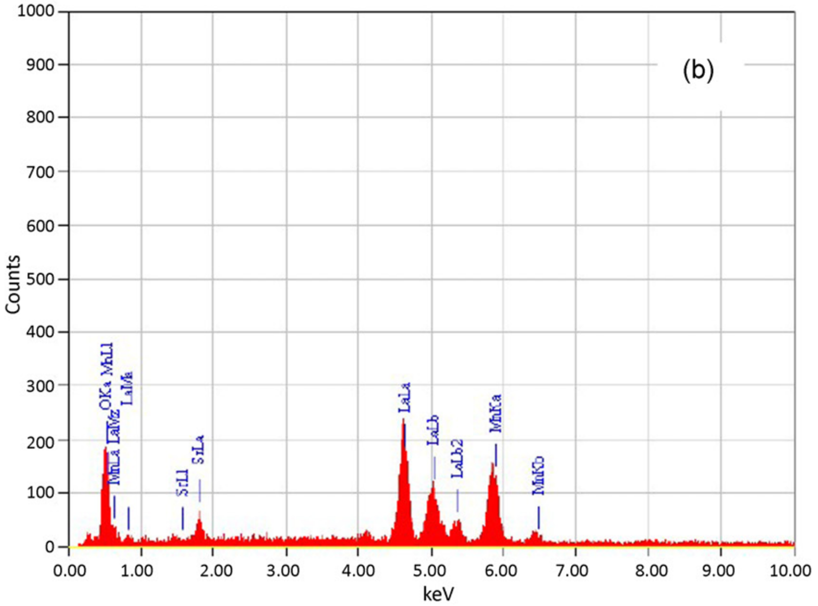

(b) sintered sample

Fig. 6. EDX pattern of and LSMO perovskite maganities.

space group of *R*3*c* along with the hexagonal structure (JCPDS file no.: 51-0409) is observed in the sample sintered at 1273 K. Nevertheless, the diffraction peaks observed in the as-prepared sample are quite broad in nature, indicating the crystalline nature. On the other hand, in sintered sample, the peaks are very narrow and slightly shifted towards its lower 2θ values which indicate the nanocrystalline nature of the sintered sample. The decrease in diffraction peak width (FWHM) for (1 1 0) planes in the sintered sample confirms the decrease in nanocrystalline size upon sintering. The observed results indicate a decrease in the crystallite size from 50 to 15 nm while comparing the sintered sample with the as-prepared sample. The estimated crystallite size for both the samples is shown in Table 1. The energy dispersive analysis of X-ray (EDAX) (Fig. 6) confirms the composition of the constituent elements present in the samples. The molar ratio of elements La, Sr, Mn and O are, respectively, 0.67, 0.32, 1 and 3 in the as-prepared, and 0.67, 0.32, 1 and 2.98 in the sintered samples. It can be noted that a reduction in oxygen ratio in the sintered sample to 2.98 from the original value of 3 in the as-prepared sample is attributed to the reduction of oxidation in atmosphere at elevated temperature during sintering. The EDAX based chemical composition values match with atomic composition of the starting materials used for preparation of perovskite materials.

Table 1
Comparison of particle size with characterisation studies.

S. No.	Parameters	Prepared	Sintered	Reference
1.	XRD – crystallite size (nm)	50	15	[8,19]
2.	SEM – grain size (nm)	60	25	[8]
3.	TEM	50	25	
4.	Structure	Rhombohedral and tetragonal	Rhombohedral	[8,19]

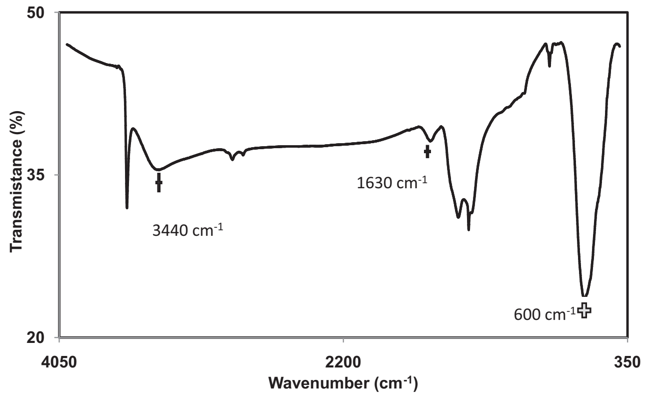

Fig. 7. Transmittance as a function of wave number in as-prepared LSMO perovskite maganities.

Table 2
FTIR spectrum observed in LSMO sample.

Wave number (cm^{-1})	Assignments	Reference
600	Stretching mode γ_s	[34]
1630	Deformation O–H bond	[35]
3440	Stretching mode O–H bond	[35]

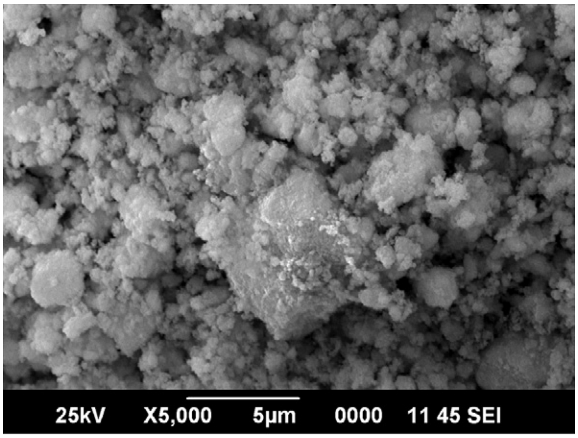

(a) As-prepared

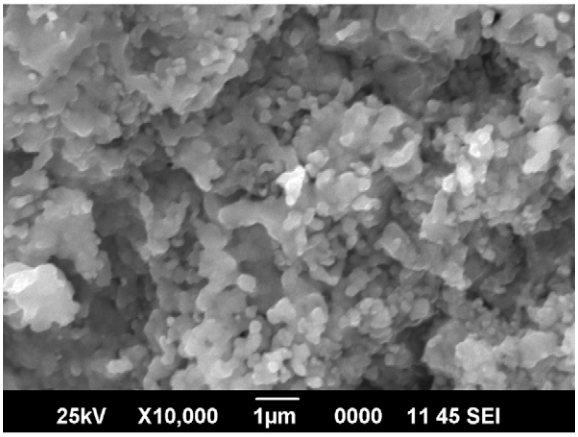

(b) Sintered sample

Fig. 8. SEM photograph of $La_{0.68}Sr_{0.32}MnO_3$ perovskite maganities.

FTIR spectrum of the as-prepared sample is given in Fig. 7. The observed band peak frequencies and the corresponding chemical group assignments are given in Table 2. The observed band at 600 cm^{-1} corresponds to γ_s stretching mode which involves the internal motion of change in Mn–O–Mn bond length [35]. The peaks observed at 1630 and 3440 cm^{-1} are assigned, respectively, to the deformation and O–H stretching mode of absorbed water molecules [36].

The SEM image of the as-prepared and sintered samples is shown, respectively, in Fig. 8. SEM micrograph of as-prepared sample reveals that the obtained LSMO samples are voluminous and porous in view of large amount of gases evolved during the sonication and preheat treatments. It is evident from Figs. 7 and 8 that the existence of irregular shapes of agglomerates along with the cage-structure in the as-prepared sample. Due to the elongated aggregates and poorly defined boundaries, the grain size determination of particles is difficult from the observed SEM images. The approximate estimate of the grain size is 60 and 25 nm, respectively, for the as-prepared and sintered samples which are shown in Table 1. It is evident from the observed XRD and FTIR results, the as-prepared sample contains a mixture of crystalline structures of rhombohedral and tetragonal [8,19] and O–H stretching mode of absorbed water molecules [36]. Thus, it reveals that an agglomerate structure with approximate grain size of 60 nm. Generally, during the sintering, the crystalline size increases while the surface area of the particles decreases. However, in the sintered sample, the particle size reduced to 25 nm due to agglomeration effect of existence of rhombohedral phase instead of mixed structure as observed in the as-prepared sample [8,19]. Therefore, a decrease in the particle size is observed in the sintered samples leads to a decrease in surface area when compared to as-prepared sample. A decrease in BET surface area is observed in the sintered sample as reported elsewhere [9,37]. The surface area measured for the as-prepared and sintered samples employing BET multiple points technique shows, respectively, 40.8 and 27.2 $m^2\,g^{-1}$. It is noted that the reduction in the surface area of the sintered sample is attributed to the agglomeration effect. The TEM images of the as-prepared and sintered samples are shown in Fig. 9(a) and (b). The estimated particle size from TEM is shown in Table 1 along with other results for comparison. The TEM studies also confirm a decrease in particle size upon sintering, as discussed earlier from the results of XRD and SEM results.

The temperature dependence of longitudinal (U_L) and shear (U_S) velocities of bulk and sintered sample are represented, respectively, in Figs. 10 and 11. Similarly, longitudinal (α_L) and shear (α_s) attenuations are plotted in Fig. 12. A gradual decrease in velocity and an increase in attenuation were observed in the temperature range 300–370 K and 380–500 K as observed in other solid material [4,27]. An anomalous behaviour is noticed at 375 K for bulk sample. The observed sharp dip in velocity and a peak in attenuation at 375 K in bulk sample is the Curie temperature (T_C) of $La_{0.68}Sr_{0.32}MnO_3$ perovskite wherein a transition from ferromagnetic to paramagnetic takes place [4–27]. In sintered samples also, an initial monotonic

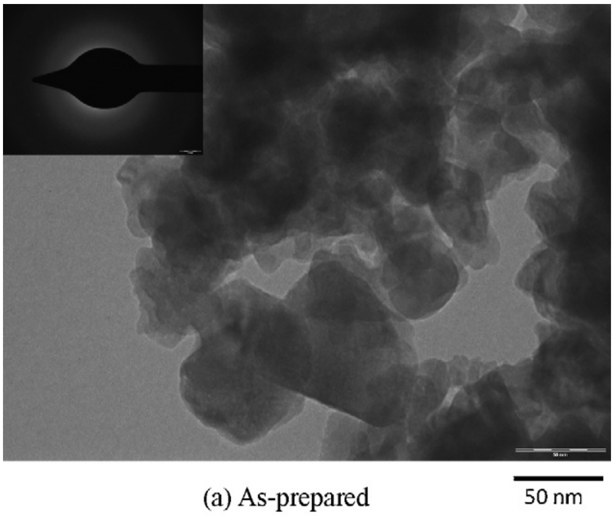

(a) As-prepared

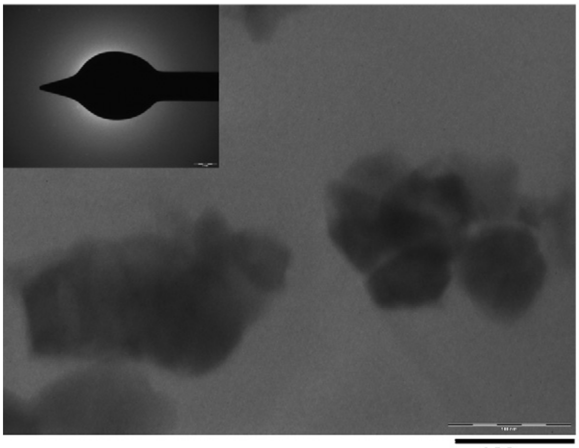

(c) Sintered sample

Fig. 9. TEM photograph of $La_{0.68}Sr_{0.32}MnO_3$ perovskite maganities.

decrease in velocities and an increase in attenuations are observed in the temperature range from 300 to 355 K. Nevertheless, it is interesting to note an anomalous behaviour in the variation of velocities and attenuations in the temperature range from 355 to 385 K. A sharp fall in velocities and a sharp increase in attenuations start at 355 K and reach the maxima/minima in their variation at 370 K. A further increase in temperature beyond 370 K leads to a sharp raise in velocities and a sharp decrease in attenuations up to 385 K. Beyond 385 K, a monotonic decrease in velocities and increase in attenuations are noticed. The shift in the peak from 375 to 370 K indicates that the T_C for the perovskite materials is shifted towards the lower value due to the sintering.

In order to get precise information on the temperature dependence of velocities and attenuations, the first differential of both the velocities (U_L and U_S) and the attenuations (α_L and α_S) as a function of temperature are plotted, respectively, in Figs. 13 and 14. The first differentials of the ultrasonic parameters are calculated by the relation ($\Delta U/\Delta T = U_2 - U_1/T_2 - T_1$ with $\Delta T = 5$ K). It is interesting to note that a more pronounced variation in magnitude in the observed minima in velocities (sharp peak) and maxima in attenuations (sharp dip) at 370 K and 375 K, respectively, for sintered and bulk sample.

Generally in any solid material, a gradual monotonic decrease in velocities and increase in attenuation with increase in temperature will be observed in the absence of any structural/phase transitions [4]. On the other hand, a pronounced peak/dip in the variation in velocities and attenuations are observed as a function of temperature which is used to explore the phase/structural transitions that take place in materials [27]. In the present study, the observed variations in velocities and attenuations as a function of temperature in the range from 300 to 500 K are used to explain the structural/phase transitions that take place in $La_{0.68}Sr_{0.32}MnO_3$ perovskite manganite materials. In most of the perovskite manganite materials, the pronounced maxima/minima in the variations in velocities and attenuations are used to correlate the existence of various magnetic transitions like Neel temperature (T_N), Curie temperature (T_C) and charge ordering temperature (T_{CO}) [4,27].

The results obtained from the ultrasonic studies in the present investigation are used to reveal the structural/phase transition in LSMO perovskite manganite materials. The anomalous dip in U_L and U_S and pronounced peak in α_L and α_S at 370 K and 375 K, respectively, for sintered sample and bulk sample are correlated with Curie temperature T_C. A comparison of the T_C value in the bulk and sintered samples is given in Table 3 along with the reported values on LSMO samples. The obtained ultrasonic parameters by on-line measurements were compared with the results obtained from other studies, as indicated in Table 3.

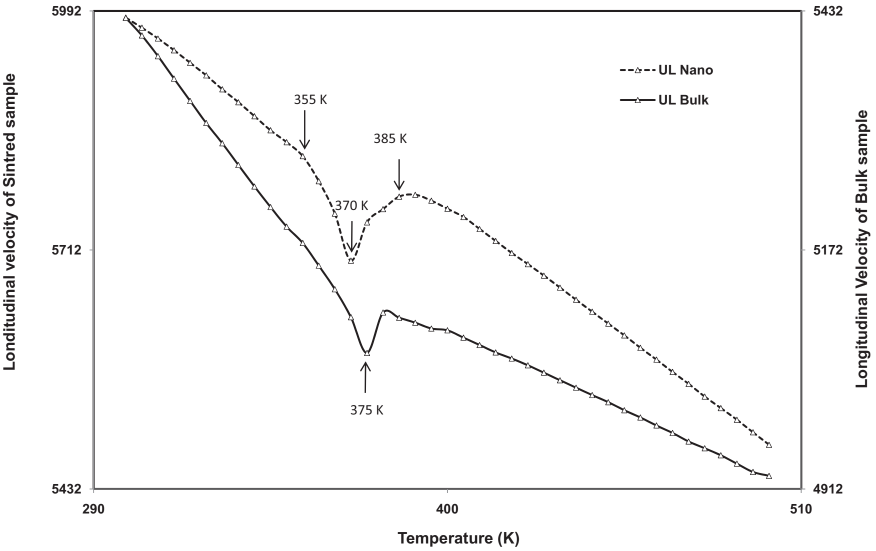

Fig. 10. Temperature dependent longitudinal velocity of sintered and bulk sample.

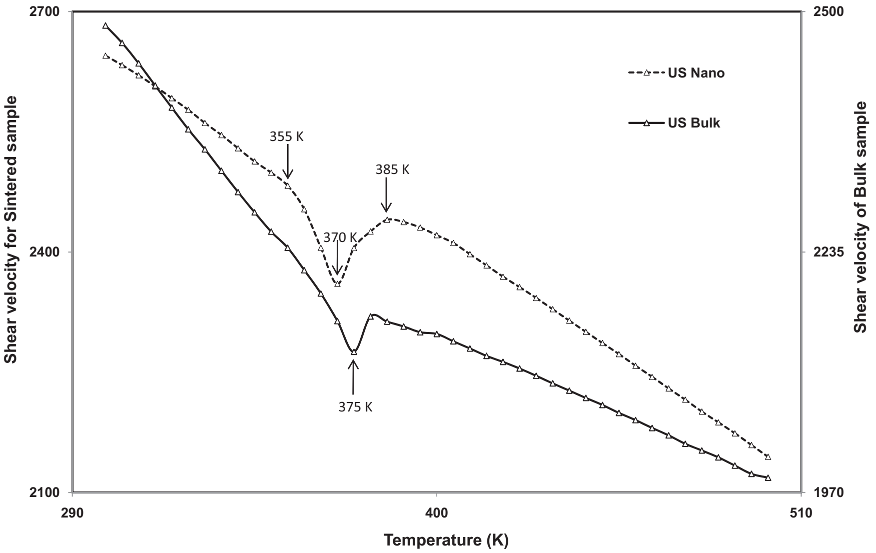

Fig. 11. Temperature dependent shear wave velocity of sintered and bulk sample.

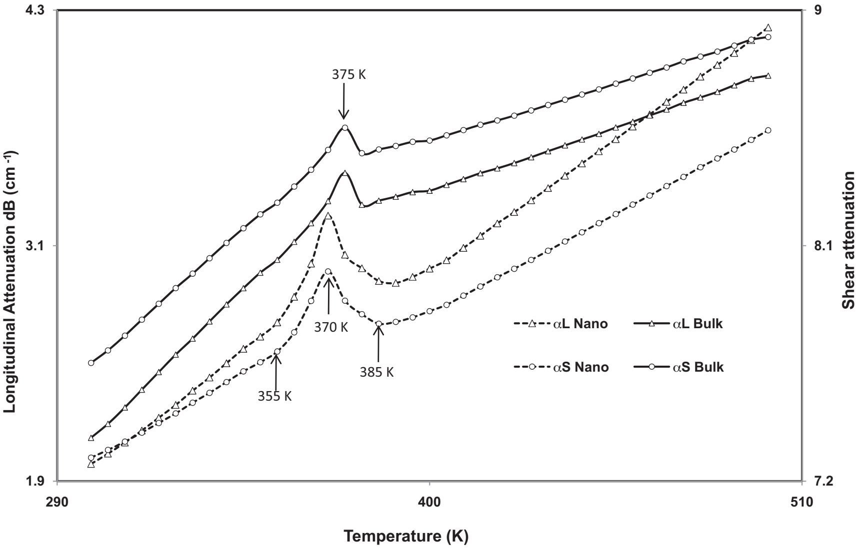

Fig. 12. Temperature dependent longitudinal and shear attenuation of sintered and bulk sample.

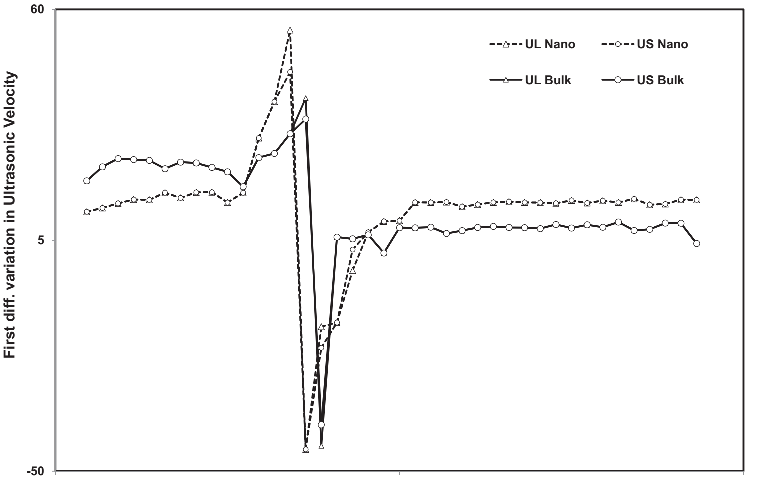

Fig. 13. Temperature dependence of first differential of longitudinal and shear velocities of sintered and bulk sample.

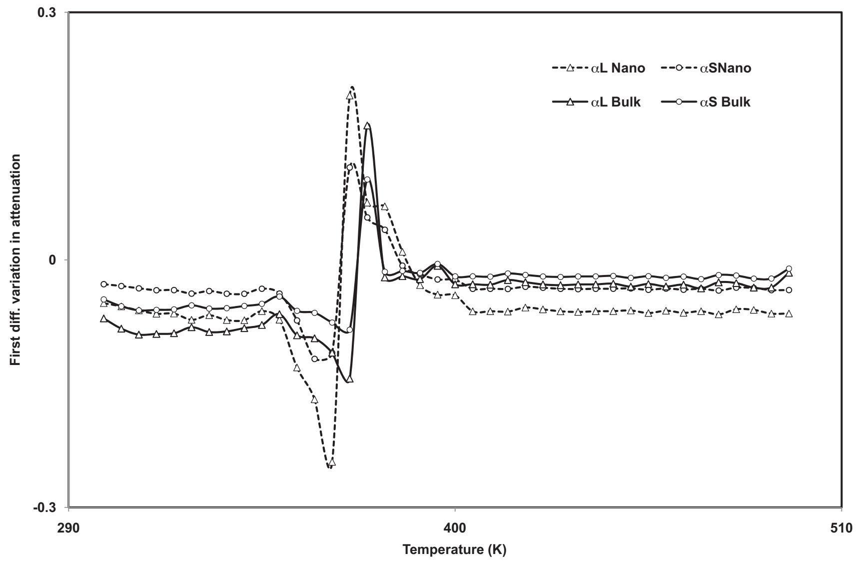

Fig. 14. Temperature dependence of first differential of longitudinal and shear attenuation of sintered and bulk sample.

Table 3
Comparison of measured ultrasonic parameters with study references.

S. No.	Parameters	Present investigation		Study reference	
		$La_{0.68}Sr_{0.32}MnO_3$		$La_{0.67}Sr_{0.33}MnO_3$ [40]	$La_{0.69}Sr_{0.31}MnO_3$ [4]
		Sintered sample	Bulk sample	Bulk sample	Bulk sample
1.	Density	5975	6235	6629.8	6676.2
2.	U_L	5984	5424.5	5896	5890
3.	U_S	2645	2484.6	2659	2654
4.	α_L	1.9879	2.1213	1.92	1.95
5.	α_S	7.29	8.019	7.27	–
6.	T_C	370 K	375 K	378 K	375 K

The interesting observation noted from longitudinal (Fig. 10) and shear (Fig. 11) velocities is that the dip at T_C is broad in nature. Further, the T_C value is shifted towards lower temperatures (370 K) in sintered sample when compared to bulk sample (375 K). The shift in T_C value after sintering is attributed to the reduction in the grain size. Attempts have been made to correlate the grain size dependent ultrasonic velocity and attenuation in stainless steel [38], Zn nanostructured materials [39], tungsten and boron carbides [40] and polycrystalline Ni–Zn ferrites [41]. Similar to U_L and U_S, α_L and α_S exhibit variation in magnitude as well as shift in peak position from 375 K to 370 K (Figs. 10–14).

The large magnitude in U_L at T_C is due to the existence of single ion (linear) magnetostriction rather than to volume magnetostriction [42]. This arises mainly due to existence of strong spin–phonon interaction in LSMO perovskite material at T_C. In the case of the volume magnetostriction effect, anomalous behaviour in longitudinal

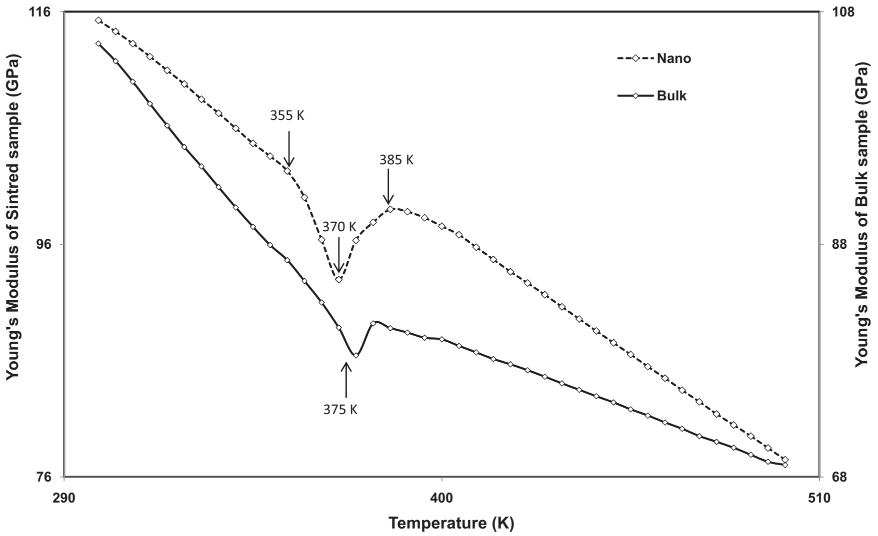

Fig. 15. Temperature dependence of Young's modulus of sintered and bulk sample.

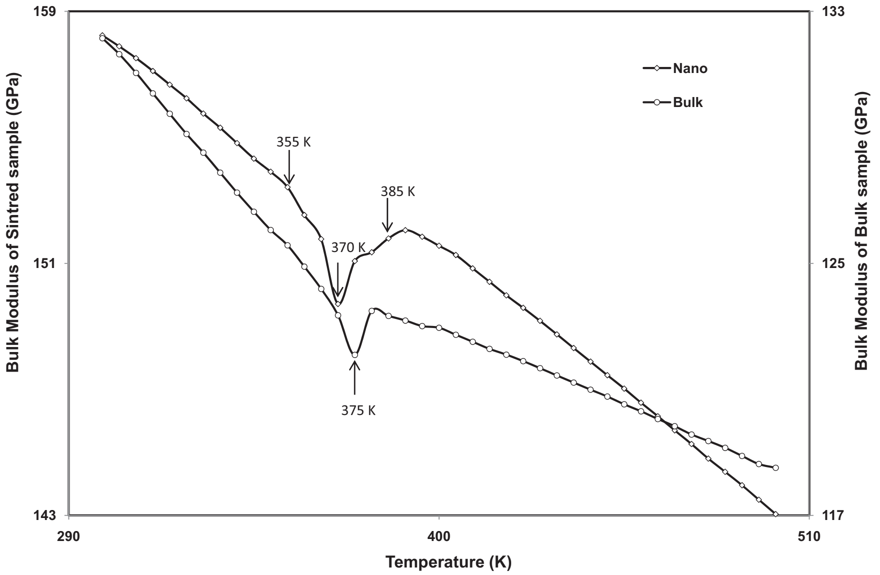

Fig. 16. Temperature dependence of Bulk modulus of sintered and bulk sample.

velocity and attenuation will exist, while shear waves do not show any anomaly [42]. The observed large variation in both U_L than U_S clearly provides the evidence for the existence of linear magnetostriction effect as observed in bulk LSMO sample [27,42,13].

The observed dramatic increase in ultrasonic velocities and decrease in attenuation with anomalous peak/dip at T_C as a function of temperature are the salient features of the present investigations. The observed sharp dip in velocities at T_C is due to occurrence of lattice softening above T_C and the lattice hardening below T_C, as noticed in our earlier studies. The observed large softening at T_C is due to transition from paramagnetic (PM) to ferromagnetic transition (FM) in LSMO perovskites [4]. The elastic moduli (Young's modulus (E) (Fig. 15) and Bulk modulus (K) (Fig. 16)) also reveal similar observations as that of velocities, both in bulk and sintered samples.

The observed start in decrease in velocity at 355 K from the conventional monotonic decrease (dotted line in Figs. 10–16) indicates that starting of the ferromagnetic (FM) transition. As the temperature increases, the transition increases and hence it reaches a maximum at 370 K wherein the perovskite is transferred from FM to paramagnetic (PM) transition. A further increase in temperature increases the transition to PM and it reaches maximum at 385 K beyond which it shows a temperature dependent uniform monotonic decrease in velocity.

Further, the observed broad variation in velocity at T_C in sintered sample than the bulk sample conforms the absence of sharp FM to PM transition, as reported [4,27]. It is also evident from the above studies that T_C is decreased to 370 K from 375 K, which is attributed to the decrease in grain size. It is inferred from earlier studies that the decrease in grain size leads to lowering in ferromagnetic transition temperature [43,44], as observed in the present investigation and there is no sharp FM to PM transition [45].

4. Conclusion

In the present investigations, the LSMO samples are prepared employing solid state reaction and sonochemical reaction. The bulk samples are sintered to obtain the nanostructured LSMO perovskite manganite materials. The characterisation studies confirm that the sintered sample is at nanoscale to a particular size of 15–30 nm. On-line ultrasonic velocity and attenuation studies on the bulk and sintered sample reveal that there is a shift in the Curie temperature (T_C) value from 375 to 370 K from the bulk to sintered sample. The shift in T_C value in the sintered sample is due to decrease in grain size of LSMO perovskites. Further, the observed broad nature of the dip in the variation of ultrasonic velocities conform the absence of sharp transition from PM to FM transition in LSMO perovskites. The observed shift in the peak in from 375 to 370 K indicates the Curie temperature (T_C) for perovskite materials is lowering due to the sintering. The observed decrease in grain size in sintered sample leads to lowering the ferromagnetic transition which is evident from the board variation in velocity at T_C. The linear magnetostriction effect is more dominate in the perovskite than volume magnetostriction effect which is evident from larger variation in both velocities (U_L and U_S). The above studies conform that on-line ultrasonic studies are more sensitive in exploring the structural/phase transitions in nanostructured perovskite manganite materials.

Acknowledgement

The authors (V.R. and K.S.) are thankful to Indira Gandhi Centre for Atomic Research (IGCAR), Kalpakkam for the financial support to carry out this research project (IGC/MMG/NDED/KSRCT/2008/2, 16.04.2008).

References

[1] G. Lalitha, D. Das, D. Bahadur, P. Venugopal Reddy, J. Alloys Compd. 464 (2008) 6.

[2] W.J. Li, W. Zhang Bo Lu, Phys. Lett. 362 (4) (2007) 327.

[3] P. Shankar, P. Mandal, A.K. Bera, S.M. Yusuf, L.S. Sharath Chandra, V. Ganesan, Phys. Rev. B 78 (2008) 012415.

[4] S. Sankar rajan, S. Aravindan, P. Manivasakan, K. Sakthipandi, V. Rajendran, J. Alloys Compd., in press.

[5] B.I. Belevtsev, G.A. Zvyasina, K.R. Zhekov, I.G. Kolobov, Panfilov, N.N. Galtsov, J. Fink, Finonicki, Appl. Phys. Lett. 88 (2006) 041920.

[6] M. Bowen, M. Bibes, A. Barthélémy, J.P. Contour, A. Anane, Y. Lemaître, A. Fert, Appl. Phys. Lett. 82 (2003) 233.

[7] R. Desfeux, S. Bailleul, A.D. Costa, W. Prellier, A.M. Haghiri-Gosnet, Appl. Phys. Lett. 78 (2001) 3681.

[8] Z.F. Zi, Y.P. Sun, X.B. Zhu, Z.R. Yang, J.M. Dai, W.H. Song, J. Magn. Magn. Matter 321 (2009) 2378.

[9] Y. Luo, I. Szafraniak, N.D. Zakharov, V. Nagarajan, M. Steinhart, R.B. Wehrspohna, J.H. Wendorff, R. Ramesh, M. Alexe, Appl. Phys. Lett. 83 (2005) 440.

[10] Z.F. Zi, Y.P. Sun, X.B. Zhu, C.Y. Hao, X. Luo, Z.R. Yang, J.M. Dai, W.H. Song, J. Alloys Compd. 477 (2009) 414.

[11] A. Rostamnejadi, H. Salamati, P. Kameli, H. Ahmadvand, J. Magn. Magn. Matter 321 (2009) 3126.

[12] T.-Y. Chen, K.-Z. Fung, J. Eur. Ceram. Soc. 28 (2008) 803.

[13] P. Kameli, H. Salamati, A. Aezami, J. Alloys Compd. 450 (2008) 7.
[14] A. Abrutis, A. Teiserskis, G. Garcia, V. Kubilius, Z. Saltyte, Z. Salciunas, V. Faucheux, A. Figueras, S. Rushworth, J. Membr. Sci. 240 (2004) 113.
[15] T.R. McGuire, A. Gupta, R.P. Duncombe, M. Rupp, J.Z. Sun, R.B. Laibowitz, W.J. Gallager, X. Gang, J. Appl. Phys. 79 (1996) 4549.
[16] E.S. Vlakhov, R.A. Chakalov, R.I. Chakalov, K.A. Nenkov, K. Dorr, A. Handstein, K.H. Muller, J. Appl. Phys. 83 (1998) 2152.
[17] Z. Yang, L. Sun, C. Ke, X. Chen, W. Zhu, O. Tan, J. Cryst. Growth 311 (12) (2009) 3289.
[18] X. Zhu, H. Shen, Z. Tang, K. Tsukamoto, T. Yanagisawa, M. Okutomi, N. Higuchi, J. Alloys Compd. 488 (2009) 437.
[19] A. Gedanken, Mater. Res. Bull. 38 (2003) 11.
[20] H.B Wang, J.F. Gao, D.K. Peng, G.Y. Meng, Mater. Chem. Phys. 72 (3) (2001) 297.
[21] C. Krishnamoorthy, K. Sethupathi, V. Sankaranarayanan, Mater. Lett. 61 (2007) 3254.
[22] L. Zhao, M. Steinhart, M. Yosef, S.K. Lee, T. Geppert, E. Pippel, R. Scholz, U. Gösele, S. Schlecht, Chem. Mater. 17 (2005) 3.
[23] V. Rajendran, N. Palanivelu, D.K. Modak, B.K. Chaudhuri, Phys. Status Solidi A 180 (2) (2000) 467.
[24] V. Rajendran, N. Palanivelu, P. Palanichamy, T. Jayakumar, B. Raj, B.K. Chaudhuri, J. Non-Cryst. Solids 296 (2001) 39.
[25] X.-S. Cao, C.-L. Chen, Phys. Lett. A 372 (32) (2008) 5356.
[26] R.K. Zheng, C.F. Zhu, X.G. Li, Phys. Status Solidi A 184 (2001) 251.
[27] S. Sankar Rajan, S. Aravindan, R. Yuvakumar, K. Sakthipandi, V. Rajendran, J. Magn. Magn. Matter 321 (21) (2009) 3611.
[28] H. Fujishiro, T. Fukase, M. Ikebe, J. Phys. Soc. Jpn. 70 (2001) 628.
[29] G. Lalitha, P. Venugopal Reddy, J. Phys. Chem. Solids 70 (2009) 960.
[30] V. Rajendran, B. Raj, P. Palanichamy, Science and Technology of Ultrasonics, Narosa Publication, New Delhi, 2004.
[31] V. Rajendran, N. Palanivelu, B.K. Chaudhuri, J. Meas. 38 (2005) 248.
[32] V. Rajendran, S. Muthukumaran, T. Jayakumar, P. Palancichamy, B. Raj, Proceeding of National Seminar of ISNT, Chennai, India, December, 5–7, 2002.
[33] V. Rajendran, K. Sakthipandi, T. Jayakumar, P. Shankar, P. Palanichamy, B. Raj, 2009 Proceedings of the Sixth International Conference on Condition Monitoring and Machinery Failure Prevention Technology, Ireland, June, 23–25, 2009, p. 1283.
[34] P. Palanichamy, P. Kalayanasundram, B. Raj, Br. J. Non-destruct. Test. 31 (2) (1989) 78.
[35] S. Roy, S. Bandyopadhyay, J. Mater. Sci. Lett. 15 (1996) 1872.
[36] M. Quijada, J. Černe, J.R. Simpson, H.D. Drew, K.H. Ahn, A.J. Millis, R. Shreekala, R. Ramesh, M. Rajeswari, T. Venkatesan, Phys. Rev. B 58 (1998) 16093.
[37] H.S. Bennett, E. Pytte, Phys. Rev. 155 (1967) 553.
[38] I. Mutlu, E. Oktay, S. Ekinci, Int. J. Micropor. Mater. Prop. 4 (2009) 423.
[39] J. Jianfeng, X. Jianrong Zhang, Y. Du, X. Zhang, Y. Li, Mater. Lett. 29 (1996) 131.
[40] I.H. Sarpun, V. Ozkan, S. Tuncel, R. Unal, Int. J. Micropor. Mater. Prop. 4 (2009) 104.
[41] S.R. Murthy, Chem. Mater. Sci. 24 (2001) 611.
[42] Z. Changfei, Z. Renkui, Phys. Rev. B 59 (1999) 11169.
[43] V. Rajendran, S. Muthukumar, V. Sivasubramanian, T. Jayakumar, B. Raj, Phys. Status Solidi A 195 (2003) 350.
[44] S. Das, P. Chowdhury, T.K. Gundu Rao, D. Das, D. Bahadur, Solid State Commun. 121 (2002) 691.
[45] L.S. Ewe, A. Imad Hamadneh, Hazar Salama, R. Abd-Shukor, Physica B 403 (2008) 2394.